# Rational Design of Dipolar Chromophore as an Efficient Dopant-Free Hole-Transporting Material for Perovskite Solar Cells

Zhong'an Li,[#] Zonglong Zhu,[#] Chu-Chen Chueh, Sae Byeok Jo, Jingdong Luo, Sei-Hum Jang, and Alex K.-Y. Jen[*]

Department of Materials Science and Engineering, University of Washington, Seattle, Washington 98195, United States

S *Supporting Information*

ABSTRACT: In this paper, an electron donor−acceptor (D-A) substituted dipolar chromophore (**BTPA-TCNE**) is developed to serve as an efficient dopant-free hole-transporting material (HTM) for perovskite solar cells (PVSCs). **BTPA-TCNE** is synthesized via a simple reaction between a triphenylamine-based Michler's base and tetracyano-ethylene. This chromophore possesses a zwitterionic resonance structure in the ground state, as evidenced by X-ray crystallography and transient absorption spectroscopies. Moreover, **BTPA-TCNE** shows an antiparallel molecular packing (i.e., centrosymmetric dimers) in its crystalline state, which cancels out its overall molecular dipole moment to facilitate charge transport. As a result, **BTPA-TCNE** can be employed as an effective dopant-free HTM to realize an efficient (PCE ≈ 17.0%) PVSC in the conventional n-i-p configuration, outperforming the control device with doped spiro-OMeTAD HTM.
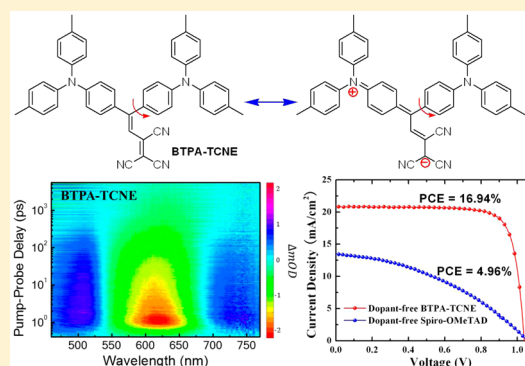
INTRODUCTION

Solution-processed hybrid lead halide perovskite solar cells (PVSCs) have presented very promising prospects as the next-generation photovoltaic technology, due to their very high power conversion efficiency (PCE), facile processability, and relatively cheap material and manufacturing cost.[1−4] Very recently, the certified PCE of state-of-the-art PVSCs has exceeded 22%.[5] This incredibly rapid progress is realized mainly due to the simultaneous development of efficient processing and fabrication of active perovskites[6,7] and suitable charge-transporting layers to facilitate efficient charge transport and collection in devices.[7−10]

Most high-performance PVSCs reported so far have been fabricated on the basis of the conventional n-i-p device configuration, in which 2,2′,7,7′-tetrakis(*N*,*N*-bis(*p*-methoxyphenyl)amino)-9,9′-spirobifluorene (spiro-OMeTAD) and its derivatives are the commonly used hole-transporting materials (HTMs).[7−14] However, the synthesis of spiro-OMeTAD-based HTMs is quite tedious and costly.[14] Moreover, an additional doping process is needed to incorporate Li-containing salts, to ensure that sufficient conductivity can be achieved for hole transport and collection.[11−17] Such a doping process not only increases the complexity of device fabrication but also induces deleterious effects on device stability due to the sophisticated oxidation procedure and undesired ion migration and interactions introduced by dopants.[18−23] Thus, it is highly desirable to develop dopant-free organic HTMs that can effectively replace spiro-OMeTAD-based HTMs.

To design dopant-free organic HTMs, one possible strategy is to employ electron donor (D)−acceptor (A) scaffolds.[23−32]

On the basis of this principle, Yang et al. have recently reported an efficient (PCE = 16.2%) PVSC using a dithienosilole (D) and 3-alkylrodanine (A)-based A-D-A-type small-molecule HTM.[23] One attractive advantage of this molecular design is that the resultant charge-transporting properties of the HTMs can be improved due to the enhanced molecular packing via strong dipole−dipole interactions. However, most of the D-A-type HTMs reported to date still require multistep synthesis and purification, which limits their widespread applications.[23−32] Alternatively, these D-A scaffolds can be easily prepared by forming dipolar push−pull chromophores, which have already been shown as potential p-type materials in organic photovoltaics and thin-film transistors.[33−36]

On the other hand, dipolar chromophores with strong intramolecular charge transfer can induce significant charge separation to form zwitterionic resonance in the ground state,[37,38] potentially providing an induced doping effect without the need to add any external dopant due to increased electron delocalization. However, such chromophores are rarely reported to function as efficient HTMs due to the lack of proper molecular design rules. The main challenge lies in designing molecules with proper zwitterionic characteristics while simultaneously maintaining efficient hole mobility, which is contradictory to the Bässler model.[39] This model states that the inherent dipolarity of a molecule has an adverse effect on charge carrier transport, and high charge carrier mobility can only be achieved for those apolar molecules.

Here, we report a new molecular design strategy of utilizing a highly dipolar D-A-type chromophore (**BTPA-TCNE**, Scheme 1) as an efficient dopant-free HTM for $CH_3NH_3PbI_3$

Scheme 1. Synthetic Route and Possible Resonance Structures of Highly Dipolar Chromophore BTPA-TCNE
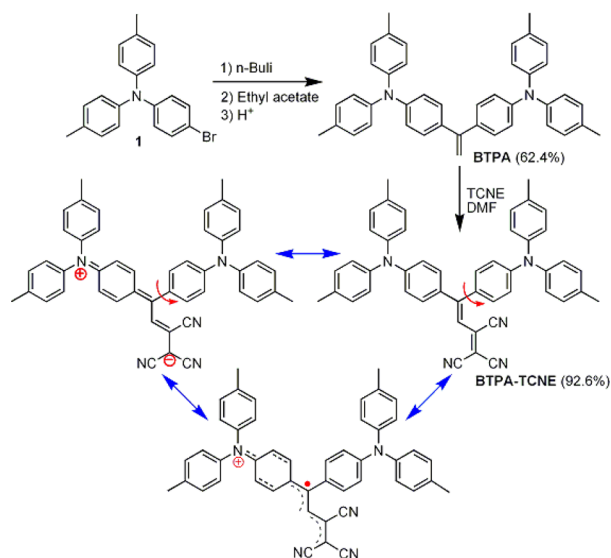
(MAPbI$_3$) PVSCs. **BTPA-TCNE** consists of triphenylamine-based Michler's base (D) and tricyanovinylene (A), possessing a strong zwitterionic resonance structure in the ground state. It also exhibits a suitable highest occupied molecular orbital (HOMO) energy level and good hole mobility due to the antiparallel molecular packing. Consequently, the derived champion PVSC using **BTPA-TCNE** as the HTM shows a very high PCE of 17.0%, outperforming most of the conventional n-i-p PVSCs reported so far using dopant-free HTM.

■ RESULTS AND DISCUSSION

The synthetic route of **BTPA-TCNE** is illustrated in Scheme 1. As shown, it only requires a straightforward two-step procedure with low synthetic complexity. The synthetic details are provided in the Experimental Section. The selection of Michler's base as the donor is due to its strong electron-donating ability that can extend the effective conjugation length of resulting chromophores to have zwitterionic resonance structure.[40–42] To obtain sufficient hole mobility of the resulting dipolar chromophore, a triphenylamine (TPA) derivative, 4-bromo-*N,N*-di-*p*-tolylaniline (**1**), was used as starting material to prepare the new Michler's base (**BTPA**) via a simple one-pot, three-step procedure with an overall yield of ∼62%. The vinyl group in **BTPA** is very electron-rich, and it can react with electron-deficient alkenes such as tetracyano-ethylene (TCNE) in DMF to give the target **BTPA-TCNE** in ∼93% yield. The tricyanovinylene is a very strong acceptor, which has the potential to stabilize the zwitterionic structure.[37,42,43] The molecular structures of both **BTPA** and **BTPA-TCNE** were fully characterized by nuclear magnetic resonance (NMR) and high-resolution mass spectra (HR-MS). The NMR spectra (Figures S24 and S25) clearly show that the two TPA units in **BTPA-TCNE** are asymmetrical, suggesting the possible spatial isomerism.

The ground-state geometric structure (monoclinic, $P\bar{1}$ space group, Table S1) of **BTPA-TCNE** can be refined by X-ray crystallography using a single crystal of **BTPA-TCNE**, obtained by slow evaporation of its chloroform/methanol solution. As shown in Figure 1, three conformational isomers can be
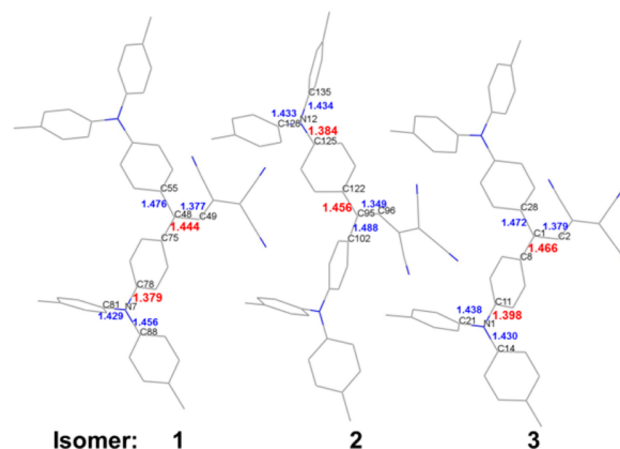

Figure 1. Three conformational isomers 1−3 in the single-crystal structure of **BTPA-TCNE**, with selected bond lengths noted. The nitrogen atoms are marked in blue and carbon atoms in gray. For clarity, the hydrogen atoms are omitted.

identified due to the rotation of one of the TPA units in the donor side, while the other one is more coplanar to the π-system. The dihedral angles between two TPA units for isomers 1−3 were measured to be 68.2°, 57.4°, and 64.7°, respectively (Figure S3). Moreover, the rotation of tricyanovinylene acceptor is also found to induce some degree of structural disorder in isomer 2.

As noted in Figure 1, the N−C$_{bridge}$ bonds between the nitrogen atom in TPA and the carbon atom in the bridging arylene group are significantly shorter (1.379 Å for N7−C78, 1.384 Å for N12−C125, and 1.398 Å for N1−C11) than those of other N−C$_{Ar}$ bonds in TPA units (1.43−1.45 Å). Besides, a clear quinoidal form can be observed in the bridging arylene group for all three isomers (Figure S4), with the calculated bond length alternation of 0.025−0.034 Å. In addition, the C−C single bonds (i.e., C48−C75 in isomer 1) connecting the arylene group to a vinyl group are slightly shorter than those connecting the twisted TPA unit to a vinyl group (i.e., C48−C55 in isomer 1). The above bond length analysis strongly suggests that the zwitterionic resonance structure can contribute to our hypothesized ground state of the designed D-A molecule (Scheme 1).[37,38]

Since there are three isomers, the molecular packing in the crystal structure of **BTPA-TCNE** is relatively complex. For example, in each unit cell (Figure S5), isomers 1 and 3 can be easily found to form a non-centrosymmetric dimer (Mode 1 in Figure 2), mostly like a dimeric J-type structure, through π-stacking between the twisted TPA unit in isomer 1 and the tricyanovinylene group in isomer 3, with a distance of 3.39 Å. When the packing structure is extended along the *b* axis (Figure 2), it is interesting to observe that isomers 1 and 3 from two adjacent unit cells can also pack into typical centrosymmetric dimers (Mode 2) through dipole−dipole interactions with a distance of ∼3.3 Å and a slippage angle of 79.7°, similar to the molecular packing reported from highly polarizable dyes such as merocyanines.[33,34] The molecular packing between isomers 1
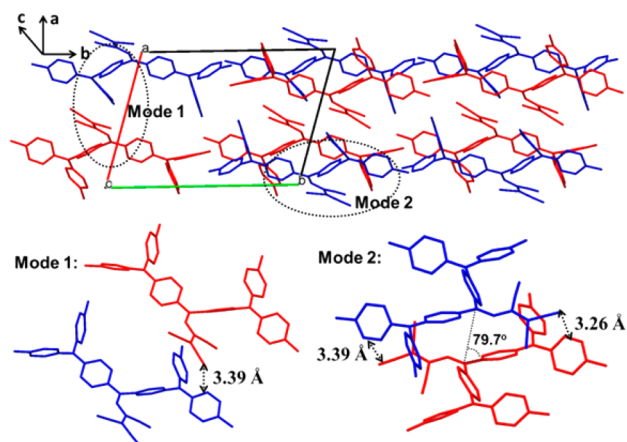
Figure 2. Two molecular packing modes between isomers 1 (blue) and 3 (red) in crystal structure of **BTPA-TCNE** viewed along the *c* axis. For clarity, the hydrogen atoms and isomer 2 are omitted.

and 2, or between isomers 2 and 3 (Figures S6 and S7), shows a trend similar to that between isomer 1 and 3. Moreover, two same neighboring isomers also pack into centrosymmetric dimers, as shown in Figure S8. All these different intermolecular interactions organically combine together to create a supramolecular structure in the solid state (Figure S9); more importantly, the formed antiparallel molecular packing can cancel out the molecular dipole moments, which will be beneficial for charge transport.[33,34,39]

An electron spin resonance (ESR) experiment on **BTPA-TCNE** powders was conducted as shown in Figure 3a, wherein
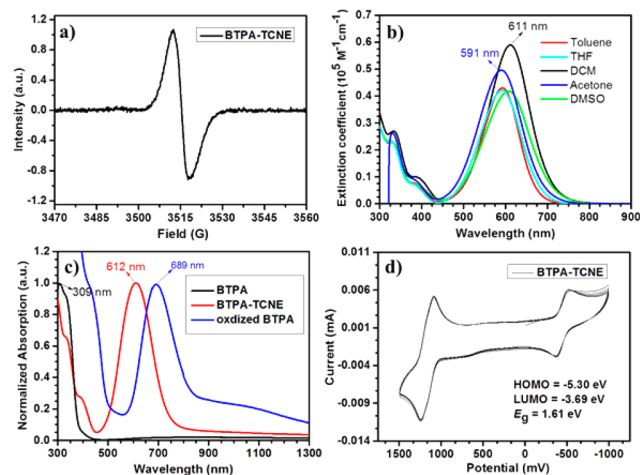

Figure 3. (a) ESR spectrum of **BTPA-TCNE** powder measured at room temperature. (b) UV−vis−IR absorption spectra of **BTPA-TCNE** in different organic solvents. (c) Film absorption spectra of **BTPA**, **BTPA-TCNE**, and oxidized **BTPA**. (d) CV curves of **BTPA-TCNE** versus Fc/Fc$^+$ (0.66 V) measured in DCM solution.

an ESR signal with a *g* value of 2.007 can be clearly seen. However, we noted that no clear trend could be detected on the basis of variable-temperature ^{1}H NMR experiments, possibly due to very low concentration of radicals generated. We conjectured those generated radical species may be stabilized by the extensively delocalized Michler's base (**BTPA**) electron donor connected to a strong electron acceptor due to the captodative effect,[44,45] with significant steric hindrance from two bulky triphenylamine units. As a

result, the combined resonance zwitterionic structure and favorable molecular packing in the solid state will facilitate efficient intermolecular charge transfer within the **BTPA-TCNE** film through coherent charge delocalization to endow efficient hole transport.

The absorption spectra of **BTPA-TCNE** in different organic solvents are shown in Figure 3b, with related data listed in Table S2. All of them show an intense and sharp absorption band in the visible region (450−800 nm), with the peak centered at ∼600 nm due to the strong intramolecular charge transfer. Typically, for the dipolar D-A chromophores, a strong positive solvatochromism will be observed when the neutral resonance structure contributes to the ground state. However, the solution spectra of **BTPA-TCNE** were found to display a weak dependence on the solvent polarity. The absorption spectra of **BTPA** before and after chemical oxidization by iodine are also shown in Figure S10 and Figure 3c for comparison, where the oxidized **BTPA** (Scheme S1) clearly exhibits a new red-shifted absorption band at 679 nm with a significant long-wavelength tail, indicating the formation of oxidized "cyanine" species associated with radical cations (Scheme S1). However, **BTPA-TCNE** cannot be further oxidized (Figure S11). In addition, the **BTPA-TCNE** is also found to be non-fluorescent. All these optical results are consistent since the ziwtterionic resonance structure plays a critical role in the ground state, as suggested by its crystal structure. The film's absorption spectra illustrated in Figure 3c showed spectral characteristics similar to those obtained in solutions (Table 1). This suggests that there is no strong

Table 1. Optical, Electrochemical, Hole Mobility, and Conductivity Properties of BTPA-TCNE and BTPA

HTM	λ_{sol}^{a} (nm)	λ_{fil}^{b} (nm)	E_{opt}^{c} (eV)	E_{HOMO}^{d} (eV)	E_{LUMO}^{e} (eV)	μ^f ($\times10^{-5}$ cm^2 V^{-1} s^{-1})
BTPA-TCNE	611	612	1.62	−5.35	−3.73	3.14
BTPA	306	309	3.18	−5.32	−2.14	1.13

^{a}Absorption maxima in DCM solutions. ^{b}Absorption maxima of thin films. ^{c}Optical band gaps calculated from film absorption edges. ^{d}Measured from UPS. ^{e}Calculated by $E_{LUMO} = E_{HOMO} + E_{opt}$. ^{f}Measured from the device structure of ITO/PEDOT:PSS/HTL/MoO$_3$/Ag.

aggregation in the solid state as a result of the steric effect from very bulky and twisted TPA-functionalized Michler's base. Furthermore, the absorption edges of **BTPA** and **BTPA-TCNE** were determined to be 390 and 766 nm, corresponding to optical band gap (E_{opt}) values of 3.18 and 1.62 eV, respectively (Table 1).

Cyclic voltammetry (CV) was employed to determine the HOMO and lowest unoccupied molecular orbital (LUMO) levels. The CV curve of **BTPA-TCNE** in DCM solution is given in Figure 3d, which displays a reversible oxidative and reductive process during several scans suggesting its good electrochemical stability. The average oxidation and reduction potentials of **BTPA-TCNE** versus Fc/Fc$^+$ were found to be 0.50 and −1.11 V, respectively, corresponding to a HOMO level of −5.30 eV and a LUMO level of −3.69 eV. To better understand the energy levels in solid-state, the HOMO levels were further measured using ultraviolet photoelectron spectroscopy (UPS), while the cutoff (E_{cutoff}) and onset (E_i) energy regions in the UPS spectra are shown in Figure 4a,b, with related data listed in Table 1. According to the equation $\phi =$
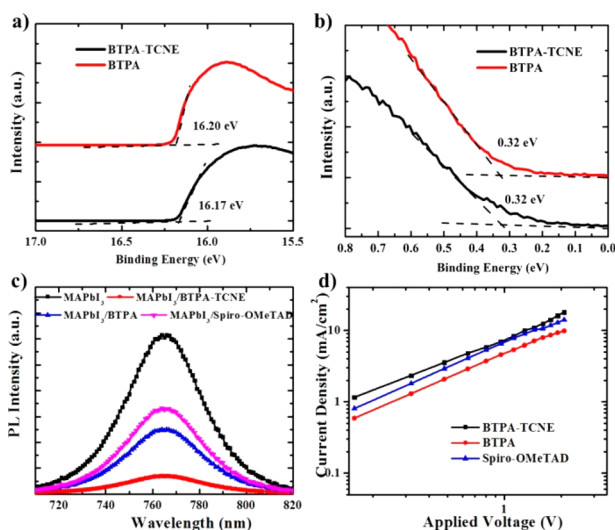
Figure 4. UPS spectra in the cutoff (a) and the onset (b) energy regions of **BTPA-TCNE** and **BTPA** films. (c) Steady-state PL spectra of the MAPbI$_3$ perovskite films with or without capping different dopant-fee HTLs. (d) Hole injection characteristics measured by the SCLC method based on the device structure of ITO/PEDOT:PSS/HTL/MoO$_3$/Ag. Note: The thin films were processed by spin-coating their 1,4-dichlorobenzene solution (10 mg/mL) onto substrates at a speed of 1000 rpm for 30 s and 4000 rpm for 20s.

21.2 − (E_{cutoff} − E_i), the HOMO levels of **BTPA-TCNE** and **BTPA** were calculated to be 5.35 and 5.32 eV, respectively. Then the LUMO levels can also be obtained as −3.73 eV for **BTPA-TCNE** and −2.14 eV for **BTPA**, respectively, by subtracting E_{opt} from HOMO levels.

The steady-state photoluminescence (PL) spectra (Figure 4c) of bi-layered MAPbI$_3$/non-doped hole-transporting layer (HTL) films were also measured to evaluate the effectiveness of charge transfer between perovskite and the studied HTLs. As can be seen, the **BTPA-TCNE**-based bilayered film shows an enhanced PL quenching compared to those of the non-doped **BTPA** and spiro-OMeTAD-based films. In general, the PL quenching is mainly due to the extraction of photoexcited charge carriers from perovskite into HTL.[46] So these results clearly indicate the better hole extraction capability of **BTPA-TCNE** relative to others. The space-charge-limited-current (SCLC) method was also employed to evaluate the hole-transporting properties of these HTMs (Figure 4d and Table 1). Hole mobility for **BTPA-TCNE** is measured to be 3.14 × 10^{-5} cm^2 V^{-1} s^{-1}, which is slightly higher than those of non-doped sipro-OMeTAD (2.13 × 10^{-5} cm^2 V^{-1} s^{-1}) and **BTPA** (1.13 × 10^{-5} cm^{2}V^{-1} s^{-1}) films. It is worth noting that the obtained hole mobility for **BTPA-TCNE** is really encouraging given its large molecular dipole moment. This can be rationalized by the formation of centrosymmetric dimers as suggested by its single-crystal structure, leading to significantly decreased overall dipole moment, therefore unrestricted by the Bässler model.

To further understand the excited-state properties, the femtosecond transient absorption (fs-TA) spectra of **BTPA-TCNE** were also studied. As shown in Figure 5a, when excited at 365 nm, **BTPA-TCNE** exhibits a photo-bleaching (PB) signal at 550−670 nm close to its steady-state absorption maximum (Figure 3c), for which it was assigned as the ground-state bleaching (GSB) signal. Two excited-state absorption (ESA) bands at 430−540 and 680−770 nm can be observed,
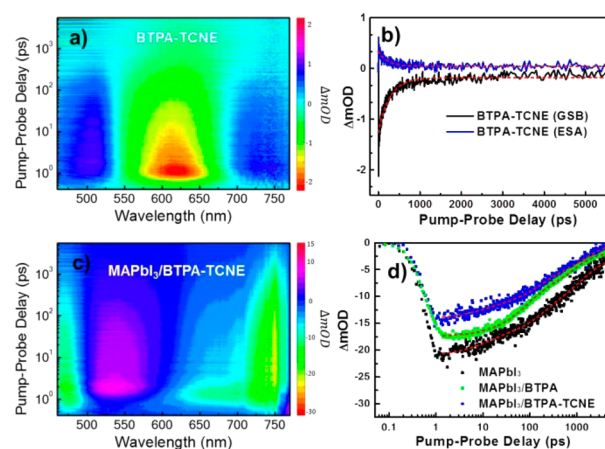

Figure 5. Femtosecond transient absorption spectra of **BTPA-TCNE** (a) and bilayered MAPbI$_3$/**BTPA-TCNE** (c) films, excited at 365 nm with 0.8 μJ/cm^2 fluence. (b) Decay curves of **BTPA-TCNE** probed at 607 (GSB) and 740 nm (ESA), respectively. (d) Decay curves of pristine perovskite and bilayer MAPbI$_3$/**BTPA** and **BTPA-TCNE** films probed at 726 nm. The decay curves were fitted by tri-exponential functions. Signals were scaled to each absorbance at pump wavelength.

while **BTPA** exhibits only broad and featureless ESA band at 450−750 nm without apparent PB signals (Figure S14). The ESA band at short wavelength suggests there is a charge-separated (CS) species at the excited state,[38] as a result of its strong dipolar structure. The decay curves for **BTPA-TCNE** probed at GSB and singlet ESA signals were best-fitted by tri-exponential functions (Figure 5b), which indicate the broad overlap of multiple emissive and non-emissive decay pathways of excited states. The GSB and singlet excited-state decay lifetimes were estimated to be 273 and 229 ps, respectively. Moreover, direct excitation of the intramolecular charge transfer absorption at 500 nm showed a similar TA spectrum and corresponding decay profiles (Figure S15). The observation of GSB and ESA bands with discrete decay behaviors can be possibly correlated to the non-emissive internal conversion process, which is consistent with steady-state fluorescent behavior as well as ESR results.

We have also further investigated the charge transfer characteristics in bilayered structures comprising of MAPbI$_3$ and HTL films. All fs-TA spectra show characteristic signals of MAPbI$_3$ perovskite films with broad PB signals at 450−500 (PB1) and 600−800 nm (PB2), as well as broad ESA signal at 500−600 nm from photo-induced refractive index changes (Figure 5c and Figure S16).[47] Although the origin of PB1 is still a subject of debate, PB2 has been well correlated to the combination of stimulated emissionand state-filling effect at the band-edge.[46,48] As shown in Figure 5d, decay profiles of PB2 scaled to PB1 in bilayered structures clearly exhibit discrete decay dynamics and quantum yields depending on the HTL, while PB1 signals from all films share strong remnant signals up until 5 ns (Figure S17). Considering that the charge-transfer process at the interface occurs over the entire time range, a low quantum yield as well as the appearance of a fast lifetime component for MAPbI$_3$/**BTPA-TCNE** could indicate the ultrafast and efficient charge transfer of photoexcited charge carriers to HTL, which is consistent with static PL results.

Devices with a typical planar n-i-p device configuration of FTO/SnO$_2$/PCBM/MAPbI$_3$/HTL/MoO$_3$/Au were fabricated to evaluate the efficacy of the **BTPA-TCNE** as dopant-free

HTM, wherein highly crystalline SnO_2 nanocrystals are used as an efficient electron-transporting layer (ETL) similar to our previous work.[49] The details of device fabrication are described in the Experimental Section. The energy-level diagram of HTMs is shown in Figure 6a, which shows their reasonably
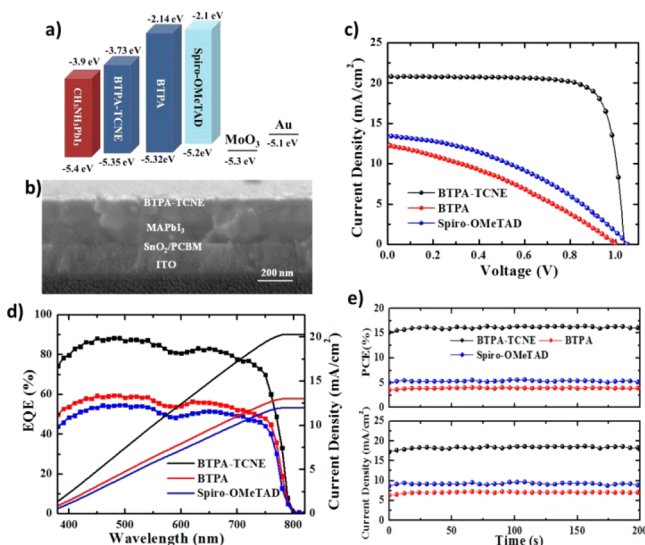

Figure 6. (a) Energy-level diagram of HTMs. (b) Cross-sectional SEM image of the device structure without top Au electrode. (c) $J–V$ curves of champion PVSCs based on the dopant-free HTMs. (d) IPCE spectra of champion PVSCs and the corresponding integrated photocurrent. (e) Stabilized PCE and photocurrent obtained while holding the cells near the maximum power point voltage at 0.89 (**BTPA-TCNE**), 0.55 (**BTPA**), and 0.58 V (spiro-OMeTAD).

matched HOMO levels with that of the valence band maximum (−5.4 eV) of MAPbI₃ to facilitate efficient hole extraction from perovskite to HTL. The cross-sectional scanning electron microscopy (SEM) image of a **BTPA-TCNE**-based cell without a top Au electrode is shown in Figure 6b, indicating the success of complete device fabrication.

The current density−voltage ($J–V$) characteristics under the AM 1.5 G irradiation at 100 mW cm^{-2} for the champion PVSCs using dopant-free HTMs are shown in Figure 6c, and the corresponding device parameters are summarized in Table 2. The champion PVSC based on the dopant-free **BTPA-TCNE** shows a very promising PCE = 16.94%, with an open-circuit voltage (V_{oc}) of 1.04, a short-circuit photocurrent (J_{sc}) of 20.84 mA cm^{-2}, and a fill factor (FF) of 0.78. This PCE outperforms most of the conventional n-i-p devices using dopant-free organic HTMs reported so far.[23−32] The PCE

Table 2. Device Parameters of MAPbI₃-Based Solar Cells Using BTPA-TCNE, BTPA, and Spiro-OMeTAD as HTMs with and without Dopants (LiTFSI + TBP)

HTM	dopants	V_{oc} (V)	J_{sc} (mA/cm^2)	FF (%)	PCE (%)
BTPA-TCNE	–	1.04	20.84	78.2	16.94
BTPA	–	1.00	13.36	33.8	4.51
spiro-OMeTAD	–	1.05	12.28	38.5	4.96
BTPA-TCNE	Li + TBP	1.06	21.06	79.2	17.68
BTPA	Li + TBP	1.01	18.03	77.3	14.07
spiro-OMeTAD	Li + TBP	1.05	20.26	73.8	15.70

histogram shown in Figure S18 reveals good reproducibility of the fabricated devices with an average PCE of ∼15.8%. In contrast, under the similar device structure and processing conditions, the reference devices using dopant-free **BTPA** and spiro-OMeTAD as HTL only yield very low PCEs of 4.51% and 4.96%, respectively, due to the significantly decreased J_{sc} and FF.

By applying the widely used chemical doping with bis-(trifluoromethane)sulfonimide lithium salt (Li-TFSI) and additive of 4-*tert*-butylpyridine (TBP),[11−17] the resulting PCE of reference devices can be significantly increased to 14.07% for **BTPA** and 15.70% for spiro-OMeTAD (Table 2 and Figure S19); however, both values are still inferior to that obtained by dopant-free **BTPA-TCNE** (∼17.0%). Moreover, we noticed that the performance enhancement by further doping **BTPA-TCNE** with Li salt and TBP is much smaller, with only a slightly higher PCE of 17.68% obtained. All these results could be attributed to the unique electronic features of **BTPA-TCNE**, whose zwitterionic resonance structure associated with small amount of resonance-stabilized radicals and the overall centrosymmetric molecular packing in solid-state favor charge delocalization, thereby facilitating efficient hole extraction and transport from perovskites to electrode.

The incident photon-to-electron conversion efficiency (IPCE) spectra (Figure 6d) of the champion devices were measured using these dopant-free HTMs, wherein the integrated J_{sc} values are consistent with those obtained from the experimental $J–V$ measurements (Table 2). Moreover, the stabilized PCE and photocurrent of the champion devices near the maximum power point were further evaluated (Figure 6e), which clearly suggest the above device performance is reliable and no apparent current hysteresis exists. The ambient stability of devices without encapsulation was also studied, and the PCE roll-off is given in Figure S20. The dopant-free **BTPA-TCNE**-based device shows improved stability compared to the doped spiro-OMeTAD devices; however, the improvement is not as significant as we initially expected, despite the absence of the chemical doping process as well as the enhanced hydrophobic nature (Figure S21) for **BTPA-TCNE**. Other factors, such as the morphology of the HTL, may play a role to affect this, and further optimization is under investigation.

CONCLUSION

In summary, a strong dipolar D-A chromophore (**BTPA-TCNE**) with good hole-transporting ability was designed and synthesized as an efficient dopant-free HTM to realize high-performance conventional n-i-p PVSCs. By combining triphenylamine-based Michler's base (as donor) and tricyano-vinylene (as acceptor), the resulting chromophore not only exhibits a zwitterionic resonance structure in the ground state but also forms antiparallel molecular packing (i.e., non-centrosymmetric dimers) in the solid state to minimize the overall molecular dipole moment. These unique features enable **BTPA-TCNE** to be an efficient dopant-free HTM for PVSCs, generating a very promising PCE of ∼17.0%. This result outperforms the control devices using doped spiro-OMeTAD HTM, and most of the dopant-free organic HTMs reported so far.

EXPERIMENTAL SECTION

Materials. Ethyl acetate was dried and distilled from CaH under an atmosphere of dry nitrogen. All chemicals and reagents were

commercially available and used as received without further purification.

Instrumentations. ^{1}H NMR and ^{13}C NMR spectra were measured using a Bruker 500 MHz instrument spectrometer. High-resolution mass spectrometry was performed by using a Thermo Linear Trap Quadrupole Orbitrap instrument, Xclaibur 2.0 DS (School of Pharmacy, UW). UV–vis–IR absorption spectra were measured using a PerkinElmer Lambda-9 spectrophotometer. The steady-state PL spectra were measured by using a Horiba Fluorolog FL-3 instrument with an excitation wavelength of 550 nm. Cyclic voltammetry was measured on a BAS CV-50W voltammetric analyzer using a conventional three-electrode cell with Pt metal as the working electrode, Pt gauze as the counter-electrode, and Ag/Ag$^+$ as the reference electrode at a scan rate of 100 mV/s. The 0.1 M solutions of tetrabutylammonium hexafluorophosphate in dichloromethane (DCM) were used as the electrolytes. Thermal transition was measured on a TA Instruments Q20-1066 differential scanning calorimeter with a heating rate of 10 °C min^{-1}. Ultraviolet photoelectron spectra were measured by a Kratos Axis Ultra DLD photoelectron spectrometer with an incident radiation of He I (21.2 eV). Transient absorption spectra were recorded using the Libra laser system (50 fs fwhm at 1 kHz repetition rate, 1 mJ/cm^2, 800 nm fundamental wavelength) combined with Helios spectrometer (Ultrafast Systems). The fundamental beam was split into two lines by a 50/50 beam splitter. Delayed probe light was generated by optical delay stage and focused on Ti:sapphire crystal to generate white continuum. The pump wavelengths of 365 and 500 nm were generated by OPerA optical parametric amplifier (Coherent, Inc.) after split of fundamental beam. Bandpass filters of 365 and 500 nm were used to eliminate residual fundamental beam. The pump fluence was modulated by two consecutive neutral density filters. The diameter of spot size was 2 mm. Morphologies were directly examined on a Sirion XL30 scanning electron microscope at an accelerating voltage of 10 kV. Aqueous static contact angle values were taken with a VCA Optima Surface Analysis System (Advanced Surface Technology Products, Billerica, MA).

Synthesis of Michler's Base (BTPA). 4-Bromo-*N,N*-di-*p*-tolylaniline (**1**, 3.09 g, 8.77 mmol) was dissolved in 20 mL of anhydrous tetrahydrofuran and cooled to −78 °C under nitrogen. Next, 3.9 mL (9.75 mmol) of butyllithium solution in hexane (2.5 M) was added dropwise slowly. After being stirred at −78 °C for 2 h, the mixture was warmed to room temperature for 15 min and then cooled to −78 °C again, and 0.43 mL (4.38 mmol) of anhydrous ethyl acetate was then added by syringe. Afterward, the mixture was kept at −78 °C for another 2 h, and then slowly warmed to room temperature for 1 h. The mixture solution was quenched with distilled water and extracted with DCM (20 mL × 3) and water (100 mL). The combined organic layer was dried over anhydrous magnesium sulfate. After removal of the solvent under reduced pressure, the residue was purified by flash column chromatography over silica gel using DCM/hexane (1:5, v/v) as eluent solvent to afford the product **BTPA** as a white solid in 62.4% yield (1.56 g). ^{1}H NMR (CDCl$_3$, 500 MHz, 298 K): δ (ppm) 2.34 (s, 12H, −CH$_3$), 5.33 (s, 2H, −C═CH$_2$−), 6.98 (d, *J* = 8.5 Hz, 4H, ArH), 7.03 (d, *J* = 8.0 Hz, 8H, ArH), 7.08 (d, *J* = 8.5 Hz, 8H, ArH), 7.22 (d, *J* = 8.5 Hz, 4H, ArH). ^{13}C NMR (CDCl$_3$, 125 MHz, 298 K): δ (ppm) 20.87, 111.50, 121.86, 124.76, 128.99, 129.92, 132.59, 134.67, 145.28, 147.80, 149.17. HR-MS (ESI): M$^+$ = 570.304 (calcd for C$_{42}$H$_{38}$N$_2$, 570.3034).

Synthesis of Dipolar Chromophore BTPA-TCNE. BTPA (114 mg, 0.20 mmol) was dissolved in 2 mL of *N,N*-dimethylformamide, and then TCNE (29 mg, 0.21 mmol) was added. The mixture was heated to 40 °C and stirred for 2 h. After the mixture cooled, 20 mL of brine was added. The precipitated blue solid was collected by filtration and washed with 30 mL of water. The crude solid was then purified by flash column chromatography over silica gel using DCM/hexane (2:1, v/v) as eluent solvent to afford the product **BTPA-TCNE** as a blue solid in 92.6% yield (125 mg). ^{1}H NMR (CDCl$_3$, 500 MHz, 298 K): δ (ppm) 2.38 (s, 6H, −CH$_3$), 2.39 (s, 6H, −CH$_3$), 6.92 (d, *J* = 9.0 Hz, 2H, ArH), 6.99 (s, 1H, −C═CH−), 7.03 (m, 4H, ArH), 7.10 (m, 8H, ArH), 7.16 (m, 8H, ArH), 7.29 (d, *J* = 9.0 Hz, 2H, ArH). ^{13}C NMR (CDCl$_3$, 125 MHz, 298 K): δ (ppm) 20.98, 21.02, 83.00, 112.38,

112.91, 113.34, 116.34, 118.63, 119.78, 126.03, 126.36, 130.29, 130.43, 132.56, 133.69, 134.56, 135.44, 143.87, 152.53, 152.62, 164.10. HR-MS (ESI): M$^+$ = 671.3043 (calcd for C$_{47}$H$_{37}$N$_5$, 671.3048).

Device Fabrication. Indium tin oxide (ITO)-coated glass substrates were cleaned with isopropanol, acetone, and distilled water sequentially and then treated with UV ozone for 20 min. Highly crystalline SnO$_2$ nanocrystals were synthesized according to the procedures used in our previous work.[49] The solution of SnO$_2$ nanocrystals was prepared by dispersing the SnO$_2$ in isopropanol and stirred overnight. The SnO$_2$ layer was prepared by spin-coating a precursor solution with a concentration of 20 mg/mL at 4000 rpm for 60 s. The PCBM ETL (10 mg/mL in chlorobenzene) was deposited by spin-coating at 3000 rpm for 30 s and 4000 rpm for 5 s. To prepare the perovskite precursor solution, CH$_3$NH$_3$I with lead(II) iodide in a molar ratio of 1:1.08 was dissolved in γ-butyrolactone and DMSO with a volume ratio of 7:3 and stirred at 60 °C overnight. The perovskite precursor solution was then spin-coated onto the above prepared substrates at 1000 rpm for 15 s and 4000 rpm for 45 s. During the last 25 s of the second spin-coating step, the substrate was treated with toluene drop-casting (0.7 mL). The as-spun films were annealed at 100 °C for ~10 min. Next, **BTPA-TCNE** or **BTPA** (10 mg/mL in 1,4-dichlorobenzene) was spin-coated on top of the perovskite layer at 2000 rpm for 30 s and 4000 rpm for 5 s, while spiro-OMeTAD (50 mg/mL in chlorobenzene) was spin-coated at 3000 rpm for 30 s and 4000 rpm for 5 s. The **BTPA-TCNE**- and **BTPA**-based devices were also annealed at 110 °C for 10 min. The chemical doping process was proceeded by adding TBP and Li-TFSI in acetonitrile solution (170 mg/mL). Finally, a 10 nm think of MoO$_3$ and 70 nm thick top Au electrode was evaporated under high vacuum (<2 × 10^{-7} Torr). For all studied devices, the device area was defined as 11.2 mm^2 by a metal shadow mask.

All the *J*−*V* curves in this study were recorded using a Keithley 2400 source measurement unit and the scan rate was kept at 0.05 V s^{-1}. The photocurrent was measured under illumination from a 450 W thermal Oriel solar simulator (AM 1.5G). The illumination intensity of the light source was accurately calibrated employing a standard Si photodiode detector equipped with a KG-5 filter, which can be traced back to the standard cell of National Renewable Energy Laboratory (NREL). The EQE spectra were measured by combining a monochromated 450 W xenon lamp (Oriel) with a sourcemeter (Keithley 2400) and calculated using a calibrated Si photodiode (OSI-Optoelectronics). Charge-carrier mobilities (μ) were calculated from the *J*−*V* characteristics using the SCLC method with the Mott−Gurney equation for the current density J_{SCLC}, expressed as $J = 9\varepsilon_r\varepsilon_0\mu V^2/8L^{31}$, where ε_0 is the vacuum permittivity, ε_r is the dielectric constant of the film, and L is the thickness of the active layer.

■ ASSOCIATED CONTENT

ⓢ Supporting Information

The Supporting Information is available free of charge on the ACS Publications website at DOI: 10.1021/jacs.6b06291.

> Reaction for the chemical oxidization of **BTPA** by iodine; crystallographic data, absorption data, and ORTEP diagram of **BTPA-TCNE**; images and data for isomers 1–3; molecular packing diagrams; absorption spectra; CV, DSC, decay, and *J*−*V* curves; water contact angles; and NMR and MS spectra of **BTPA** and **BTPA-TCNE**, including Scheme S1, Tables S1 and S2, and Figures S1–S27 (PDF)

> X-ray crystallographic data for **BTPA-TCNE** (CIF)

■ AUTHOR INFORMATION

Corresponding Author
*ajen@u.washington.edu

Author Contributions
#Z.L. and Z.Z. contributed equally to this work.

■ REFERENCES

(1) Green, M. A.; Ho-Baillie, A.; Snaith, H. J. *Nat. Photonics* **2014**, *8*, 506.

(2) Williams, S. T.; Rajagopal, A.; Chueh, C. C.; Jen, A. K-Y. *J. Phys. Chem. Lett.* **2016**, *7*, 811.

(3) Meng, L.; You, J.; Guo, T.-F.; Yang, Y. *Acc. Chem. Res.* **2016**, *49*, 155.

(4) Docampo, P.; Bein, T. *Acc. Chem. Res.* **2016**, *49*, 339.

(5) NREL. Best Research-Cell Efficiencies. http://www.nrel.gov/ncpv/images/efficiency_chart.jpg, accessed August, 2016.

(6) Sharenko, A.; Toney, M. F. *J. Am. Chem. Soc.* **2016**, *138*, 463.

(7) Seo, J.; Noh, J. H.; Seok, S. I. *Acc. Chem. Res.* **2016**, *49*, 562.

(8) Chueh, C.-C.; Li, C.-Z.; Jen, A. K-Y. *Energy Environ. Sci.* **2015**, *8*, 1160−1189.

(9) Yu, Z.; Sun, L. *Adv. Energy Mater.* **2015**, *5*, 1500213.

(10) Ameen, S.; Rub, M. A.; Kosa, S. A.; Alamry, K. A.; Akhtar, M. S.; Shin, H.-S.; Seo, H.-K.; Asiri, A. M.; Nazeeruddin, M. K. *ChemSusChem* **2016**, *9*, 10.

(11) Kim, H.; Lim, K.-G.; Lee, T.-W. *Energy Environ. Sci.* **2016**, *9*, 12.

(12) Liu, M.; Johnston, M. B.; Snaith, H. J. *Nature* **2013**, *501*, 395.

(13) Jeon, N. J.; Lee, H. G.; Kim, Y. C.; Seo, J.; Noh, J. H.; Lee, J.; Seok, S. I. *J. Am. Chem. Soc.* **2014**, *136*, 7837.

(14) Yang, W. S.; Noh, J. H.; Jeon, N. J.; Kim, Y. C.; Ryu, S.; Seo, J.; Seok, S. I. *Science* **2015**, *348*, 1234.

(15) Gratia, P.; Magomedov, A.; Malinauskas, T.; Daskeviciene, M.; Abate, A.; Ahmad, S.; Graetzel, M.; Getautis, V.; Nazeeruddin, M. K. *Angew. Chem., Int. Ed.* **2015**, *54*, 11409.

(16) Saliba, M.; Orlandi, S.; Matsui, T.; Aghazada, S.; Cavazzini, M.; Correa-Baena, J.-P.; Gao, P.; Scopelliti, R.; Mosconi, E.; Dahmen, K.-H.; De Angelis, F.; Abate, A.; Hagfeldt, A.; Pozzi, G.; Graetzel, M.; Nazeeruddin, M. K. *Nat. Energy* **2016**, *1*, 15017.

(17) Xu, B.; Bi, D.; Hua, Y.; Liu, P.; Cheng, M.; Grätzel, M.; Kloo, L.; Hagfeldt, A.; Sun, L. *Energy Environ. Sci.* **2016**, *9*, 873.

(18) Hawash, Z.; Ono, L. K.; Raga, S. R.; Lee, M. V.; Qi, Y. *Chem. Mater.* **2015**, *27*, 562.

(19) Wang, Y.-K.; Yuan, Z.-C.; Shi, G.-Z.; Li, Y.-X.; Li, Q.; Hui, F.; Sun, B.-Q.; Jiang, Z.-Q.; Liao, L.-S. *Adv. Funct. Mater.* **2016**, *26*, 1375−1381.

(20) Franckevičius, M.; Mishra, A.; Kreuzer, F.; Luo, J.; Zakeeruddin, S. M.; Grätzel, M. *Mater. Horiz.* **2015**, *2*, 613.

(21) Kazim, S.; Ramos, F. J.; Gao, P.; Nazeeruddin, M. K.; Grätzel, M.; Ahmad, S. *Energy Environ. Sci.* **2015**, *8*, 1816.

(22) Huang, C.; Fu, W.; Li, C.-Z.; Zhang, Z.; Qiu, W.; Shi, M.; Heremans, P.; Jen, A. K.-Y.; Chen, H. *J. Am. Chem. Soc.* **2016**, *138*, 2528.

(23) Liu, Y.; Hong, Z.; Chen, Q.; Chen, H.; Chang, W.-H.; Yang, Y.; Song, T.-B.; Yang, Y. *Adv. Mater.* **2016**, *28*, 440.

(24) Kim, G.-W.; Kang, G.; Kim, J.; Lee, G.-Y.; Kim, H. I.; Pyeon, L.; Lee, J.; Park, T. *Energy Environ. Sci.* **2016**, *9*, 2326.

(25) Bi, D.; Mishra, A.; Gao, P.; Franckevičius, M.; Steck, C.; Zakeeruddin, S. M.; Nazeeruddin, M. K.; Bäuerle, P.; Grätzel, M.; Hagfeldt, A. *ChemSusChem* **2016**, *9*, 433.

(26) Liu, Y.; Hong, Z.; Chen, Q.; Chang, W.; Zhou, H.; Song, T.-B.; Young, E.; Yang, Y.; You, J.; Li, G.; Yang, Y. *Nano Lett.* **2015**, *15*, 662.

(27) Liu, Y.; Chen, Q.; Duan, H.-S.; Zhou, H.; Yang, Y.; Chen, H.; Luo, S.; Song, T.-B.; Dou, L.; Hong, Z.; Yang, Y. *J. Mater. Chem. A* **2015**, *3*, 11940.

(28) Cheng, M.; Chen, C.; Yang, X. C.; Huang, J.; Zhang, F. G.; Xu, B.; Sun, L. C. *Chem. Mater.* **2015**, *27*, 1808.

(29) Steck, C.; Franckevičius, M.; Zakeeruddin, S. M.; Mishra, A.; Bäuerle, P.; Grätzel, M. *J. Mater. Chem. A* **2015**, *3*, 17738.

(30) Qin, P.; Paek, S.; Dar, M. I.; Pellet, N.; Ko, J.; Grätzel, M.; Nazeeruddin, M. K. *J. Am. Chem. Soc.* **2014**, *136*, 8516.

(31) Zheng, L.; Chung, Y.-H.; Ma, Y.; Zhang, L.; Xiao, L.; Chen, Z.; Wang, S.; Qu, B.; Gong, Q. *Chem. Commun.* **2014**, *50*, 11196.

(32) Heo, J. H.; Im, S. H.; Noh, J. H.; Mandal, T. N.; Lim, C.-S.; Chang, J. A.; Lee, Y. H.; Kim, H.-j.; Sarkar, A.; Nazeeruddin, M. K.; Grätzel, M.; Seok, S. I. *Nat. Photonics* **2013**, *7*, 486.

(33) Arjona-Esteban, A.; Krumrain, J.; Liess, A.; Stolte, M.; Huang, L.; Schmidt, D.; Stepanenko, V.; Gsänger, M.; Hertel, D.; Meerholz, K.; Würthner, F. *J. Am. Chem. Soc.* **2015**, *137*, 13524.

(34) Zitzler-Kunkel, A.; Lenze, M. R.; Schnier, T.; Meerholz, K.; Würthner, F. *Adv. Funct. Mater.* **2014**, *24*, 4645.

(35) Cho, M. J.; Seo, J.; Oh, H. S.; Jee, H.; Kim, W. J.; Kim, K. H.; Hoang, M. H.; Choi, D. H.; Prasad, P. N. *Sol. Energy Mater. Sol. Cells* **2012**, *98*, 71.

(36) Huang, F.; Chen, K.-S.; Yip, H.-L.; Hau, S. K.; Acton, O.; Zhang, Y.; Luo, J.; Jen, A. K.-Y. *J. Am. Chem. Soc.* **2009**, *131*, 13886.

(37) Getmanenko, Y. A.; Hales, J. M.; Balu, M.; Fu, J.; Zojer, E.; Kwon, O.; Mendez, J.; Thayumanavan, S.; Walker, G.; Zhang, Q.; Bunge, S. D.; Brédas, J.-L.; Hagan, D. J.; Van Stryland, E. W.; Barlow, S.; Marder, S. R. *J. Mater. Chem.* **2012**, *22*, 4371.

(38) Zeng, Z.; Lee, S.; Son, M.; Fukuda, K.; Burrezo, P. M.; Zhu, X.; Qi, Q.; Li, R.-W.; Navarrete, J. T. L.; Ding, J.; Casado, J.; Nakano, M.; Kim, D.; Wu, J. *J. Am. Chem. Soc.* **2015**, *137*, 8572.

(39) Hertel, D.; Bässler, H. *ChemPhysChem* **2008**, *9*, 666.

(40) Yang, Y.; Wang, H.; Liu, F.; Yang, D.; Bo, S.; Qiu, L.; Zhen, Z.; Liu, X. *Phys. Chem. Chem. Phys.* **2015**, *17*, 5776.

(41) Wu, Y.; Bureš, F.; Jarowski, P. D.; Schweizer, W. B.; Boudon, C.; Gisselbrecht, J.-P.; Diederich, F. *Chem. - Eur. J.* **2010**, *16*, 9592.

(42) Gawel, P.; Wu, Y.; Finke, A. D.; Trapp, N.; Zalibera, M.; Boudon, C.; Gisselbrecht, J.-P.; Schweizer, W. B.; Gescheidt, G.; Diederich, F. *Chem. - Eur. J.* **2015**, *21*, 6215.

(43) Lambert, C.; Gaschler, W.; Schmälzlin, E.; Meerholz, K.; Bräuchle, C. *J. Chem. Soc., Perkin Trans. 2* **1999**, *2*, 577.

(44) Viehe, H. G.; Janousek, Z.; Merényi, R.; Stella, L. *Acc. Chem. Res.* **1985**, *18*, 148.

(45) Pasto, D. J. *J. Am. Chem. Soc.* **1988**, *110*, 8164.

(46) Xing, G.; Mathews, N.; Sun, S.; Lim, S. S.; Lam, Y. M.; Grätzel, M.; Mhaisalkar, S.; Sum, T. C. *Science* **2013**, *342*, 344.

(47) Price, M. B.; Butkus, J.; Jellicoe, T. C.; Sadhanala, A.; Briane, A.; Halpert, J. E.; Broch, K.; Hodgkiss, J. M.; Friend, R. H.; Deschler, F. *Nat. Commun.* **2015**, *6*, 8420.

(48) Manser, J. S.; Kamat, P. V. *Nat. Photonics* **2014**, *8*, 737.

(49) Zhu, Z.; Bai, Y.; Liu, X.; Chueh, C.-C.; Yang, S.; Jen, A. K.-Y. *Adv. Mater.* **2016**, *28*, 6478.